Carbon Trends 8 (2022) 100186

Contents lists available at ScienceDirect

Carbon Trends

journal homepage: www.elsevier.com/locate/cartre

Shock wave propagation in carbon honeycomb nanostructure and effect of cell vacancies

Jiaqi Li[a], Lichun Bai[b], Wei He[a], Bo Liu[a,*], Qihong Fang[a], Kun Zhou[c]

[a] College of Mechanical Vehicle Engineering, Hunan University, Changsha 410082, Hunan, China
[b] Key Laboratory of Traffic Safety on Track, Ministry of Education, School of Traffic & Transportation Engineering, Central South University, Changsha 410075, China
[c] School of Mechanical and Aerospace Engineering, Nanyang Technological University, 50 Nanyang Avenue, Singapore 639798, Singapore

ARTICLE INFO

Article history:
Received 6 March 2022
Revised 16 June 2022
Accepted 16 June 2022

ABSTRACT

Due to its periodic porous structure and high mechanical strength, carbon honeycomb (CHC), a new carbon allotrope, possesses a high energy absorption capability and thus great potential for the design and fabrication of advanced impact-resistant materials. In this work, the propagation and attenuation of shock waves in CHC are investigated for the first time via molecular dynamics simulation. The simulation results indicate that the propagation speed of shock waves in CHC is highly anisotropic and the shock wave energy decays with the propagation distance exponentially regardless of the direction. In addition, the energy decay is accelerated at elevated temperatures. When vacancies are introduced into CHC, the shock wave propagation in it is significantly impeded due to the large deformations of the vacancies in the form of shrinkage and expansion caused by the shock wave. The calculation of the critical shock wave intensity at which structure failure of CHC initiates shows that the cell axis direction of CHC can sustain a high shock wave intensity which is over two times higher than those for the other two directions. The simulation results obtained in this work are helpful for the design, fabrication, and application of CHC-based and other porous impact-resistant materials.

1. Introduction

Tough and impact-resistant materials are highly demanded in situations wherein high-speed collisions must be shielded, and these materials are widely adopted in various engineering applications, such as aircrafts, automobiles, electromechanical devices, and personal protective equipment. When subjected to shock waves, these materials can absorb their kinetic energy and retard their propagation via severe plastic deformation, vibration mitigation, and stress redistribution. Common impact-resistant materials that have been developed so far mainly include fiber composites, cellular and porous materials, magnetorheological fluids, metallic tubes, sandwich structures, lattice and truss structures, and functionally graded structures [1–3]. Among them, cellular materials have attracted intensive research interest due to their high energy absorption capability (EAC) and unique plateau stress-strain responses [4–9].

Recently, carbon honeycomb (CHC), a new carbon allotrope with a stable 3D hexagonal porous structure, was synthesized experimentally by Krainyukova *et al.* [10] via the deposition of vacuum-sublimated graphite. CHC was theoretically proposed by Karfunkel *et al.* [11] early in 1992 and can be regarded as a periodic cellular network consisting of graphene (GE) nanoribbons that are connected at their edges by a line of sp^3 hybridized carbon atoms to form an array of hexagonal pillars. Theoretical investigations have demonstrated that CHC possesses excellent mechanical and physical properties [12–18], and thus holds great promise in various practical applications like liquid/gas storage and transport [19–21], electrodes in ion batteries and supercapacitors [22,23].

Based on density function theory calculations, Pang *et al.* [12] and Gu *et al.* [16] reported that the tensile strength of CHC along its cell axis direction can be as high as ~70 GPa and that in the honeycomb armchair or zigzag direction can also reach a high value of ~40 GPa. In addition, a superior ductility with a fracture strain of over 30% has been observed in the armchair direction. Due to the porous structure of CHC, it has a low mass density and its specific strength is superior to those of most engineering materials including metals, lightweight carbon nanotube arrays, and

* Corresponding author.
E-mail address: boliu@hnu.edu.cn (B. Liu).

https://doi.org/10.1016/j.cartre.2022.100186

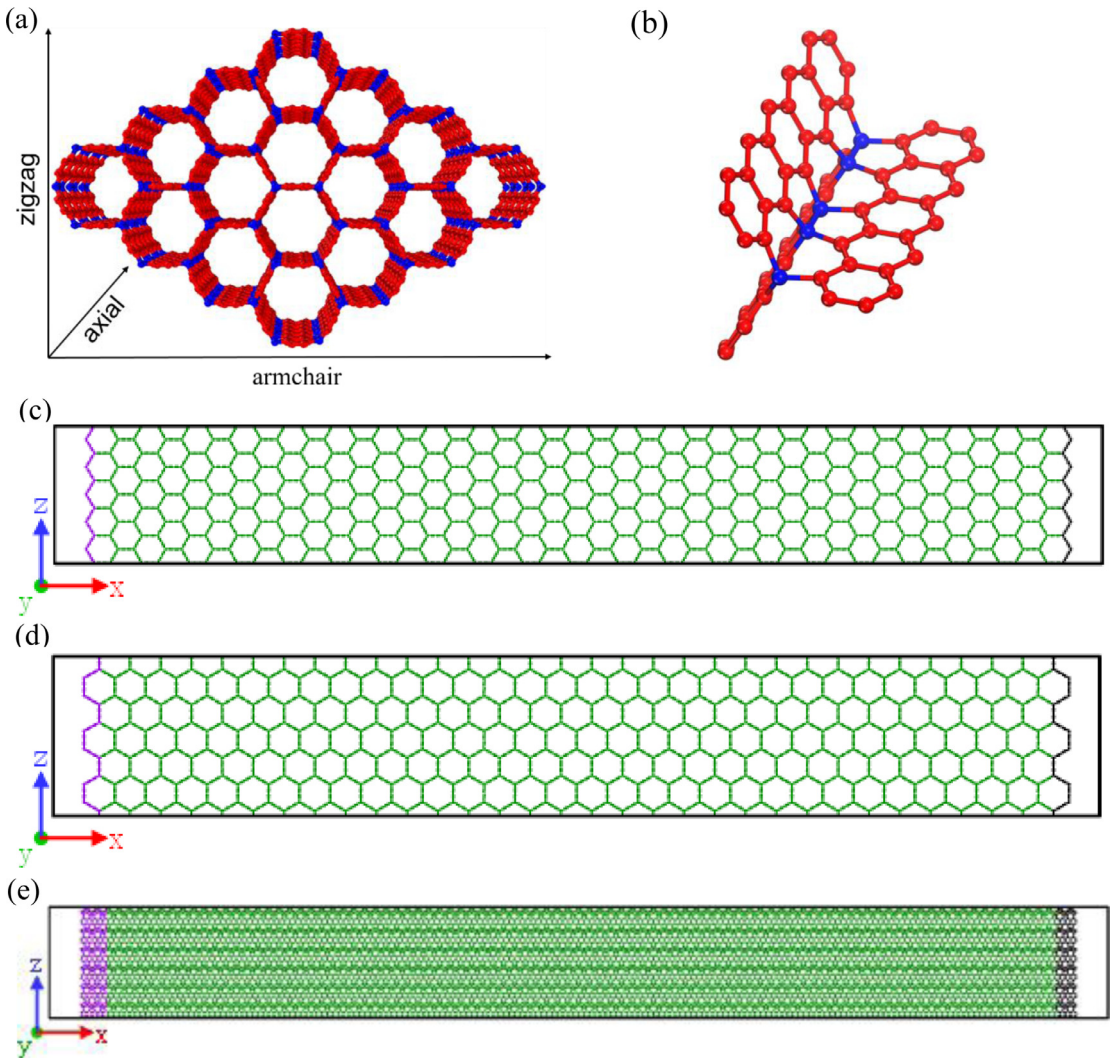

Fig. 1. Atomic structures of (a) a CHC supercell and (b) a triple junction at the vertex of a honeycomb cell in CHC. The carbon atoms at the junctions (colored blue) are sp^3 hybridized, while the other carbon atoms (colored red) are sp^2 hybridized. The MD simulation models of CHC under shock loading in the armchair, zigzag, and axial direction are shown in parts (c-e), respectively. The atoms colored in purple at the left end are set to possess an artificially large initial velocity in the *x*-direction to generate the shock wave, and the atoms colored in black at the right end are fixed in place. The black solid square represents the boundary of the simulation box.

GE-based nanocomposites [12]. By conducting molecular dynamics (MD) simulation, Yi *et al.* [7] studied the EAC of CHC under compressive loading and reported that the EAC of CHC prior to failure initiation can reach 1310 and 1570 J/g in the armchair and zigzag directions, respectively. The EAC further increases to 2180 J/g when the compressive loading is applied in the cell axis direction. The remarkably high EAC observed in CHC is orders of magnitude higher than those of conventional cellular energy absorption materials, such as steel foams and aluminum foams (with EAC in the range of 1–100 J/g). These previous studies demonstrate that CHC is a promising impact-resistant material and possesses great potential in high-speed collision shielding.

However, the current studies on the mechanical properties of CHC mainly rely on its tensile or compressive response, and the impact resistance of CHC is only estimated by calculating its EAC based on the compressive stress-strain curve. To fully characterize the impact resistance of a material, the propagation and attenuation of shock waves in it should also be investigated. Hence, this work is devoted to investigating the shock wave propagation and attenuation in CHC via MD simulation. The effects of cell vacancy defects and temperature on the impact resistance of CHC are also studied.

2. Simulation method

The atomic structure of CHC is shown in Fig. 1(a), which can be considered as a periodic array of honeycomb cells each of which consists of six identical GE nanoribbons with their longer sides aligned in the cell axis direction. The triple junction at a vertex of a honeycomb cell in CHC can be formed either by connecting three armchair-edged GE nanoribbons or three zigzag-edged nanoribbons, with the zigzag-edged nanoribbons leading to a slightly higher mechanical strength of CHC [16]. Hence, in this study, the zigzag-edged nanoribbons are adopted to construct the CHC structure. For each two GE nanoribbons that are in connection, the atomic structure at their junction region can be viewed as an array of periodic units each of which consists of two pentagonal carbon rings and one octagonal carbon ring, as shown in Fig.1(b). Upon the formation of the triple junctions, the carbon atoms at the edges of the nanoribbons (colored blue) are sp^3 hybridized, while the other carbon atoms (colored red) remain sp^2 hybridized.

In practical applications, an impact-resistant material may get shocked in any direction. Hence, it is necessary to investigate the orientation dependence of the shock response of CHC. In this study, MD simulations are conducted to investigate the shock wave at-

tenuation and propagation in CHC in the armchair, zigzag, and cell axis directions, and the corresponding simulation models are shown in Fig. 1(c-e), respectively, with their dimensions of the simulation box set at 374.88×14.76×49.19 Å^3, 334.49×14.76×51.12 Å^3, and 487.08×9.84×51.12 Å^3. The MD simulations are conducted with the Large-scale Atomic/Molecular Massively Parallel Simulator (LAMMPS) package [24] and the simulation results are visualized using the OVITO package [25]. The adaptive intermolecular reactive empirical bond order (AIREBO) potential with a set of modified cutoff parameters [26] is adopted to describe the atomic interactions.

The CHC structure is first energy-minimized by using the conjugate gradient method with periodic boundary conditions applied in all the three directions. The system is then thermally equilibrated at a preset temperature and the atmospheric pressure in the isothermal-isobaric (NPT) ensemble for 300 ps with a time step of 1 fs using the Nosé-Hoover thermostat and barostat [27,28]. Four temperature values (1, 100, 300, and 500 K) are considered to investigate the effect of temperature on the shock wave attenuation.

Upon reaching the equilibrium state, the system is switched to the microcanonical (NVE) ensemble. The periodic boundary condition that applied in the *x*-direction is removed, whereas those applied in the other two directions are retained. A vacuum layer with a thickness of 20 Å is placed at both the left and right ends of the simulation model to provide space for the structure deformation induced by the shock wave. Meanwhile, a thin layer of carbon atoms at the right end (colored black in Fig. 1(c-e)) is freezed to mimic a reflective boundary. To generate the shock wave, an artificially high velocity in the shock direction is assigned to the carbon atoms in a thin layer at the left end of the CHC structure which is denoted as the shock wave activation region (colored purple in Fig. 1(c-e)). Afterward, the simulation system is allowed to evolve with time freely during which the dynamic behaviors of representative carbon atoms and the kinetic energy of the system are investigated to detect the shock wave propagation and attenuation in CHC.

The carbon atoms at the triple junctions are selected as the representative atoms for the simulation models shown in Fig. 1(c) and (d) where the shock wave is generated to propagate in the armchair and zigzag directions, respectively. In the simulation model shown in Fig. 1(e) where the shock wave propagates in the cell axis direction, the carbon atoms on a set of *y*-*z* planes that are equally separated by a distance of 14.76 Å (corresponding to the width of six zigzag dimer lines in GE) from the left end of the simulation box are adopted as the representative atoms. For all the three simulation models, the representative carbon atoms that have the same initial *x*-coordinate are distributed to the same group for the averaging purpose. All the groups are numbered in sequence based on the ascending order of the *x*-coordinate of their constitutive carbon atoms.

3. Results and discussion

3.1. Propagation and attenuation of shock waves in perfect CHC

When subjected to impact loadings with high intensities, solids could undergo severe plastic deformation and present liquid-like deformation behaviors, which can lead to a large number of defects and material failure. Hence, to investigate the shock wave propagation and attenuation in perfect CHC, the mechanical response of CHC under the effect of the shock wave is limited to the elastic range by setting the initial velocity of the atoms in the shock wave activation region at 2.6 km/s, a value at which the structural transformation or failure of CHC is prevented. This initial velocity corresponds to an initial shock wave energy of 126.11, 151.345, and 176.58 eV for the three simulation models shown in Fig. 1(c-e), respectively. Here, the shock wave energy is calculated as the total kinetic energy of excited atoms in the activation region after subtracting their kinetic energy at thermal equilibrium.

Fig. 2(a-c) show the time-dependent displacements in the first few picoseconds of the representative carbon atoms in the *x*-direction at 1 K for the shock waves propagating in the armchair, zigzag, and cell axis directions, respectively. The displacements of the representative atoms at 1 K are analyzed because their random thermal vibrations are significantly suppressed at this temperature and their displacements are mainly activated by the shock wave. Their displacements at higher temperatures (i.e., 100, 300, and 500 K) can be found in Supplementary Fig. S1 of the supplementary material.

After the shock wave reaches the right fixed end, it is reflected and the initially displaced atoms first move back to their original positions and then displace in the reflecting direction of the shock wave, as indicated by the group-averaged displacements in a longer period of 50 ps of the representative carbon atoms for the shock wave propagating in the armchair direction (Supplementary Fig. S2). This propagation -reflection process repeats cyclically until the shock wave energy is completely dissipated in the CHC structure. Due to the dissipation of the shock wave energy, the maximum displacements of the atoms induced by the shock wave reduce gradually as the shock wave propagates in the CHC structure.

Each curve in the figures corresponds to the averaged displacement of a group of representative atoms with the same initial *x*-coordinate. It can be observed that the carbon atoms are activated by the shock wave to displace in a sequence of their *x*-coordinates. Once the atoms in each group reach their maximum displacements, they do not return to their original equilibrium positions but vibrate around their maximum displacement positions. In addition, both the displacements and the vibration amplitudes of the carbon atoms are much larger for the shock waves propagate in the armchair and zigzag directions than those for the cell axis direction. Furthermore, when the shock wave propagates in the armchair or zigzag direction, the maximum displacements of the carbon atoms decrease as their *x*-coordinates increase, indicating that the CHC structure is compressed by the shock wave. Particularly, the decrease of the displacement is more prominent for the zigzag direction, which is a sign of the more efficient damping of the shock wave energy in this direction.

A unique feature of the shock wave that propagates in the armchair direction is that its propagation speed is not constant. As exemplified by the time-dependent displacement curves of the atoms in the 1st, 2nd, and 3rd groups (Fig. 2(a)), the time of the shock wave propagation from the 1st group to the 2nd group is much longer than the propagation time from the 2nd group to the 3rd group, although the projection distance in the shock wave propagation direction (i.e., *x*-direction) between the 1st and 2nd groups is shorter than that between the for the 2nd and 3rd groups. This observation demonstrates that shock wave propagation is much faster in the GE nanoribbons that are in parallel to the wave propagation direction.

Despite the variable local propagation speed of the shock wave in the armchair direction, the global propagation speed across the whole CHC structure in this direction is almost identical to that in the zigzag direction. Specifically, the global wave propagation speed is calculated by $v=L/t$ in this work, where L and t denote the length of the CHC structure and the time required for the shock wave to reach its right end, respectively. The simulation results indicate that the average propagation speed in the armchair, zigzag, and cell axis directions are 11.46 km/s, 11.47 km/s, and 25.91 km/s, respectively. This result is in good consistency with the simulation results reported by Zhang *et al.* [15] and Gu *et al.* [16] that the stiffnesses (Youg's moduli) in the armchair and zigzag directions are identical but much lower than that in the cell axis direction since

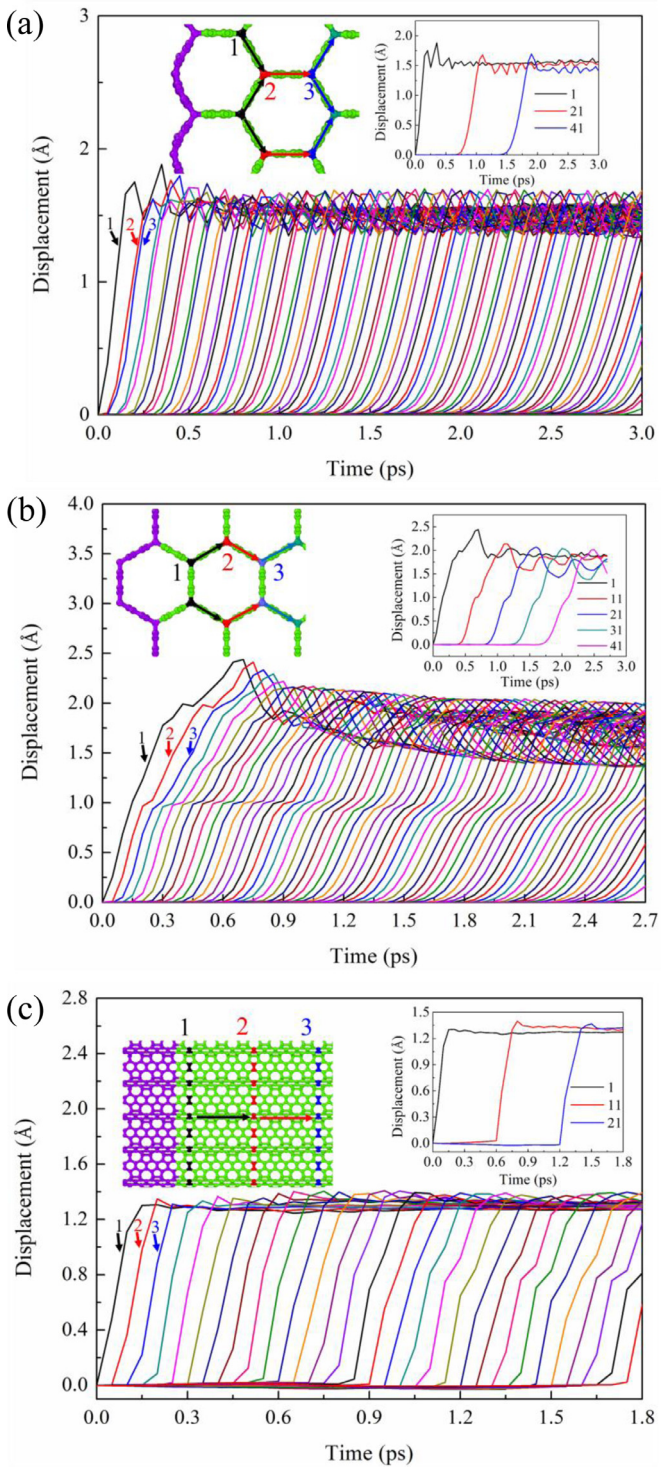

Fig. 2. The group-averaged displacements of the representative carbon atoms in the *x*-direction at 1 K for the shock waves propagating in the (a) armchair, (b) zigzag, and (c) cell axis direction. The inset on the top left of each part shows the first three groups of the representative carbon atoms (labeled by 1, 2, and 3 and colored in black, red, and blue, respectively) with the shock wave propagation pathway being highlighted by the arrows. The inset on the top right of each part shows the averaged displacements of a subset of the groups of the representative carbon atoms to provide a clearer view of their displacements.

it is generally known that the transmission speed of a mechanical wave in a solid material is positively proportional to its stiffness. It is worth mentioning that the propagation speed of the shock wave changes slightly with the increase of temperature because of the low sensitivity of the stiffness of CHC towards temperature (see Supplementary Fig. S3).

To quantitatively characterize the capability of CHC in damping the shock wave propagation in different directions, the evolution of residual energy $E(x)$ of the shock wave as it propagates in the CHC structure is investigated and plotted in Fig. 3(a-c). Here, the residual energy $E(x)$ at the propagation distance x is estimated by the increase of the total energy of all the atoms that stay in front of the shock wave (i.e., all the atoms with coordinates larger than x) after the shock wave passes through the position x. It is observed that for all the three propagation directions, the residual energy $E(x)$ of the shock wave decays with the propagation distance x in an exponential pattern which can be fitted to the functional form of $E(x)=a\exp(-bx)$, as shown by the fitting curves delineated by the solid lines.

In addition, the residual energy of the shock wave that propagates in the zigzag direction decays the most rapidly, regardless of the temperature. For instance, at 300 K, the power exponent parameter b for the zigzag direction is ~0.0095, which is significantly higher than those of ~ 0.008 and ~ 0.002 for the armchair and cell axis directions, respectively. The more rapid decay of the shock wave energy in the zigzag direction than the armchair direction is in good agreement with the results reported by Li *et al.* [29] who studied the vibration and damping characteristics in a CHC-based resonator subjected to periodic harmonic excitation. Their simulation results also indicate that the damping factor in the zigzag direction is higher than that in the armchair direction. The more rapid decay of the shock wave energy in the zigzag direction can be attributed to the fact that one-fifth of the GE nanoribbons are perpendicular to the shock wave propagation direction and separated by the pores of CHC. Hence, these perpendicular nanoribbons impose a higher impedance on the shock wave transmission and result in a higher decaying rate of the shock wave energy in the zigzag direction.

With the increase of temperature, the decay of the residual energy of the shock wave becomes increasingly rapid, as demonstrated by the monotonic increase of the power exponent parameter b with temperature (Fig. 3(d)). In addition, the temperature dependences of the parameter b for the armchair and zigzag directions are much more prominent than that for the cell axis direction. As the temperature increases from 1 K to 300 K, the parameter b increases by ~3 times from 0.00303 to 0.0114 for the armchair direction and from 0.00469 to 0.01202 for the zigzag direction, whereas it only increases by ~2 times from 0.00101 to 0.00235 for the cell axis direction. This result indicates that increasing temperature is more efficient in enhancing the impact resistance of CHC in the armchair and zigzag directions than in the cell axis direction.

A possible reason for the prominent temperature dependence of the shock wave attenuation in the armchair and zigzag directions can be ascribed to the enhanced thermal vibration of the carbon atoms at high temperatures because of the low stiffness in these two directions. With the increase of temperature, the carbon atoms displace more and more out of step from each other when the shock wave propagates in the armchair or zigzag direction, and the corresponding displacement curves also become more disordered and present enhanced fluctuations, particularly after the atoms reach their maximum displacements (see Supplementary Fig. S1). As the vibrations of the atoms turn to be increasingly random, the directional transport of the shock wave is largely disturbed. Consequently, a higher decaying rate of the shock wave energy is observed.

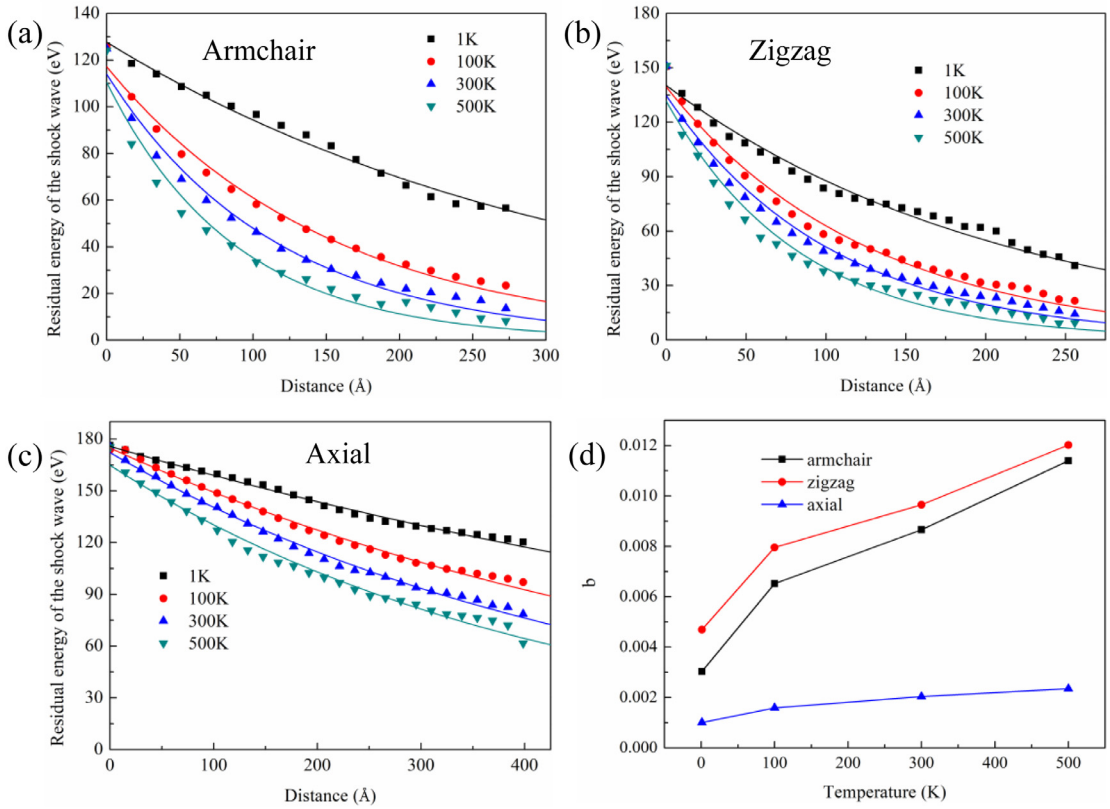

Fig. 3. Residual energy $E(x)$ of the shock wave as a function of its propagation distance x for the (a) armchair, (b) zigzag, and (c) cell axial directions. The symbols represent the residual energy obtained from the MD simulation, while the solid lines represent the exponential fitting curves. (d) Dependence of the power exponent parameter b of the exponential fitting on temperature.

3.2. Propagation and attenuation of shock waves in CHC containing vacancies

The CHC structure investigated so far is considered to be ideally perfect. However, various types of defects are usually inevitable during the fabrication of nanomaterials. Previous studies have demonstrated that cell vacancies can lead to significant effects on the thermal and mechanical properties of CHC [30]. Hence, in this section, the effect of cell vacancies on the propagation and attenuation of the shock waves in CHC is studied.

Since the focus of this section is the effect of cell vacancies, only the shock wave propagates in the armchair direction is modeled. Three defective CHC models are constructed to contain 1, 2, and 3 cell vacancies, respectively. The vacancy is created by deleting a triple junction of the CHC and its associated three GE nanoribbons. For each model, the vacancies are evenly distributed along the shock wave propagation direction in the left half of the CHC structure while the right half is kept intact. With this defect distribution, the distance of two adjacent vacancies is small and the attenuation of the shock wave traveling between them can be limited to a low level. As a result, a high residual energy of the shock wave can be retained each time it passes through a vacancy and the effect of vacancies on shock wave propagation can be effectively studied. Fig. 4(a) shows the MD simulation model containing three cell vacancies.

When the shock wave passes through the cell vacancies, they undergo severe shrinkage and expansion deformation, as indicated by the evolutions of the local atomic structures in their vicinities (Fig. 4(b)). The deformations of the vacancies occur through the significant bending of the GE nanoribbons at the edges of the cell vacancies. Since their bending deformation consumes energy, the shock wave propagation is impeded, which can be further illustrated by the displacement curves of the representative carbon atoms for the defective CHC structure containing three vacancies, as shown in Fig. 5.

It is observed that the carbon atoms on the right of each vacancy take a longer time to reach their maximum displacements than the atoms on the left of the vacancy, and the corresponding magnitudes of the maximum displacements are also lower for atoms on the right. Hence, apparent downward and leftward shifts of the displacement curves occur at the locations of the vacancies, resulting in large “voids” among the displacement curves. In addition, as the shock wave propagates through the vacancies, their shrinkage and subsequent expansion deformation drags and pushes the atoms around them, leading to intensive vibrations of these atoms. This phenomenon is most prominent for the carbon atoms on the left of the first cell vacancy which presents the largest deformation because the shock wave possesses the highest kinetic energy at the beginning of its propagation in the CHC structure.

The effect of the vacancies on the shock wave propagation can further be characterized by the evolutions of the residual energy $E(x)$ of the shock wave as it propagates across the CHC structures containing various numbers of cell vacancies at different temperatures, as shown in Fig. 6(a-c). The evolution of $E(x)$ in the perfect CHC structure is replotted for comparison purposes.

At all the temperatures considered, the decay of $E(x)$ keeps the exponential manner that is observed for the perfect CHC structure. In addition, the decaying rate of $E(x)$ is enhanced with the increase of cell vacancies and such enhancement is the most prominent when the defect number increases from 0 to 1. At 1 K, the fitted power exponent parameter b increases by ~3 times from 0.003 to 0.009 when one vacancy is created in CHC. As the vacancy number increases from 1 to 3, the parameter b increases by

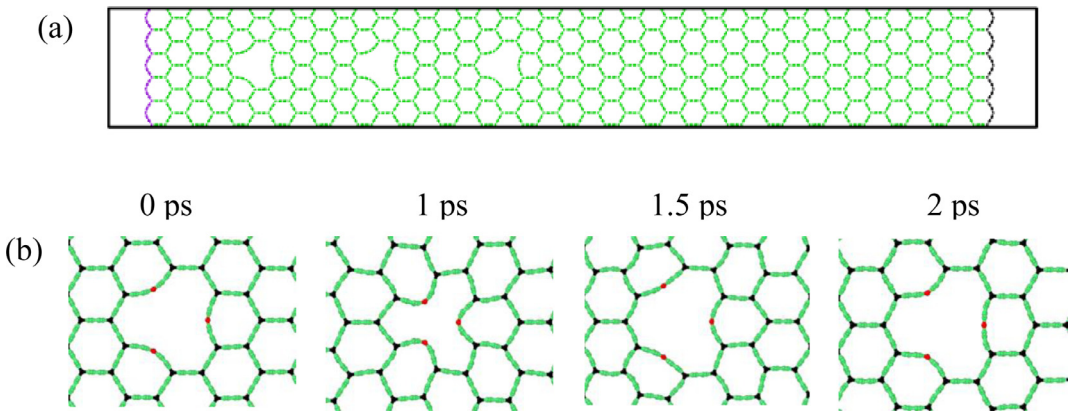

Fig. 4. (a) MD simulation model of the CHC structure containing three cell vacancies that are evenly distributed in the left half of the structure. (b) Evolution of the local atomic structures in the vicinity of a vacancy defect as the shock wave passes through it. The atoms colored in black denote the sp^3 hybridized carbon atoms located at the triple junctions of three GE nanoribbons, while the atoms colored in red denote the sp^2 hybridized carbon atoms located at the double junctions of two GE nanoribbons that form the edges of the cell vacancies.

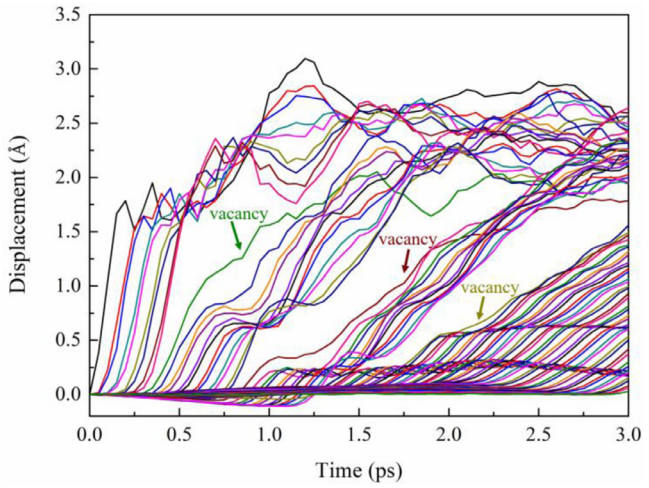

Fig. 5. Evolution of the group-averaged displacements in the *x*-direction of the representative carbon atoms at 1 K for the shock wave propagating in the armchair direction of CHC structure containing three cell vacancies. The arrows indicate the displacements of the groups of carbon atoms of which the initial *x*-coordinates align with the centers of the vacancies.

only 50% (Fig. 6(d)). Furthermore, at elevated temperatures, the effect of cell vacancies on the shock wave propagation is weakened. For instance, at 500 K, the parameter *b* increases by only 60% when three cell vacancies are created in the CHC structure. These results indicate that increasing the porosity of CHC is beneficial in enhancing its impact-resistance, buth the enhancement is most promiant when the porosity is low and is also limited by the temperature.

It is noted that the vacancies in the simulation models are perfectly aligned in the shock wave propagation direction. To shed light on the effect of the arrangement of vacancies on the shock wave attenuation, two additional defective CHC models each containing two vacancies in the left half are constructed (Supplementary Fig. S4). The two vacancies are shifted with respect to each other in a direction normal to that of the shock wave propagation with certain offset distances. The simulation results show that the offset distance does not significantly affect the shock wave attenuation (Supplementary Fig. S5).

However, in the present simulation model, the periodic boundary conditions are applied in the directions perpendicular to that of the shock wave propagation and the separation distances among vacancies are set at the same constant. As a result, the vacancies can be considered to be uniformly distributed without local concentrations. When the vacancies are arranged randomly, there might be local areas with high vacancy concentrations which could have a significant effect on the shock wave attenuation and deserve a further study.

3.3. Critical shock wave intensity for CHC structure collapse

In the previous discussion, the shock wave intensity (defined as the shock wave energy per unit area in this study) is limited to a low value of 0.176 eV/Å^2 by setting the initial velocity of the atoms in the shock wave activation region at 2.6 km/s. The CHC structure responds elastically to the shock wave and there is no any local structure collapse or fracture induced by the shock wave. Limiting the response of CHC structure to shock waves in the elastic range is beneficial to keep the integrality of the structure such that it can retain its attenuation toward sustained or periodic shocks. However, severe structure collapse is required to achieve the high EAC of CHC as revealed by the study of its mechanical response under compressive loading [7]. Hence, it is of great importance to study the critical shock wave intensity at which structure collapse is initiated in CHC.

To achieve this goal, the shock wave intensity applied in the MD simulation model is increased gradually by increasing the initial velocity of the atoms in the activation region from 2.6 km/s with an increment of 0.1 km/s. The critical shock wave intensity is obtained when local structure collapse is initiated in the CHC structure. Fig. 7 shows the local atomic structure of CHC with local structural failure and its atomic stress distribution after the shock wave with an intensity of 0.51 eV/Å^2 (corresponding to an initial velocity of 4.4 km/s for the atoms in the activation region) propagates in the armchair direction for 1.3 ps. Because of the high shock wave attenuation in the armchair direction, a large portion of the initial shock wave energy is retained in the activation region, leading to severe local atomic structure distortion and high atomic stresses in this region. Analysis of the local atomic structure distortion shows that the structure collapse of CHC occurs through both bond breaking and forming.

The critical shock wave intensities for the armchair, zigzag, and cell axis directions at different temperatures are plotted in Fig. 8. With the increase of temperature, the critical shock wave intensity decreases monotonically. This phenomenon can be attributed to the reduced mechanical strength of CHC [13] and the enhanced random thermal vibrations of the carbon atoms at elevated tem-

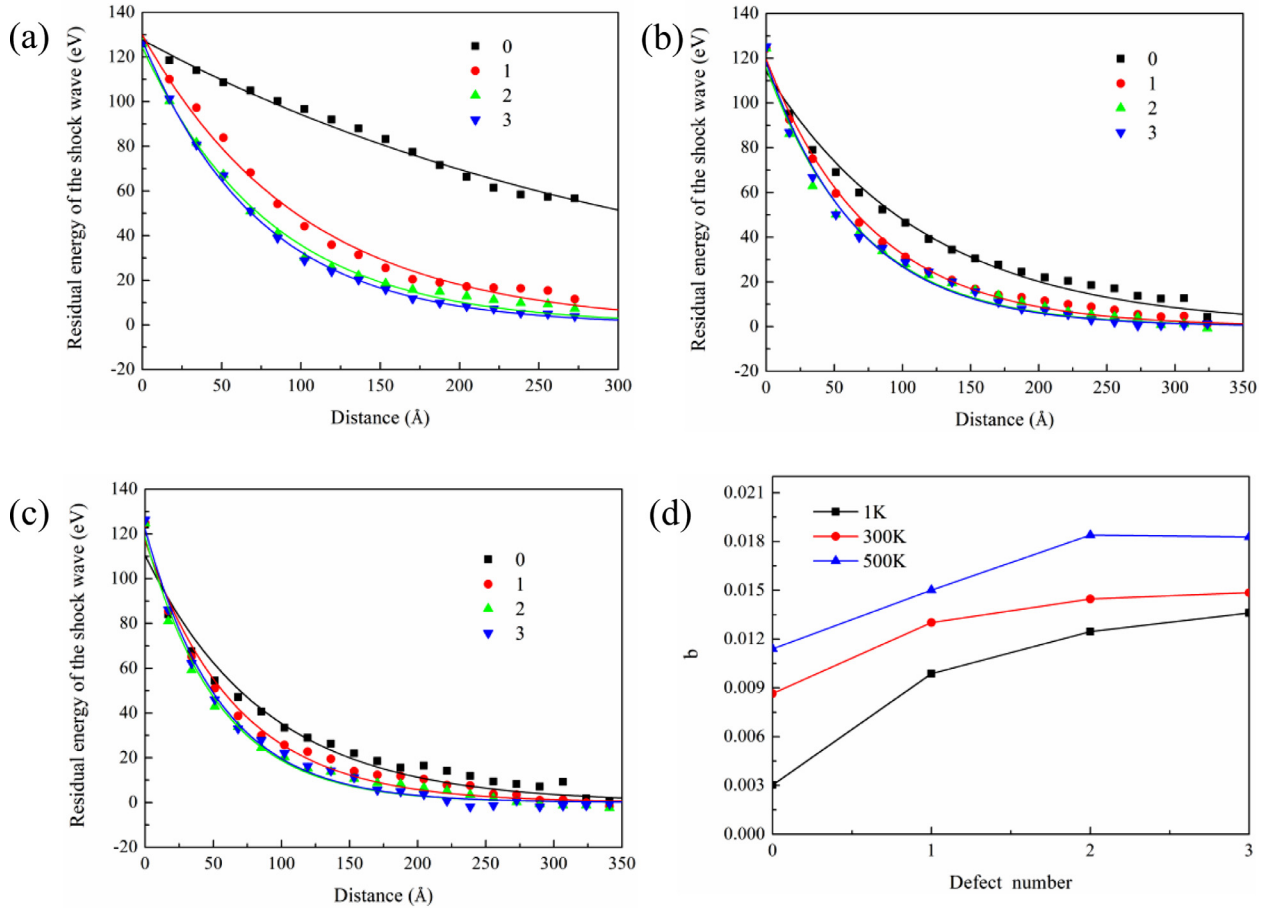

Fig. 6. Evolutions of the residual energy $E(x)$ of the shock wave as it propagates in CHC containing various numbers of cell vacancies at (a) 1 K, (b) 300 K, and (c) 500 K. (d) Dependence of the fitted power exponent parameter b on the number of vacancy defects at different temperatures. The labels 0, 1, 2, and 3 denote the numbers of defects.

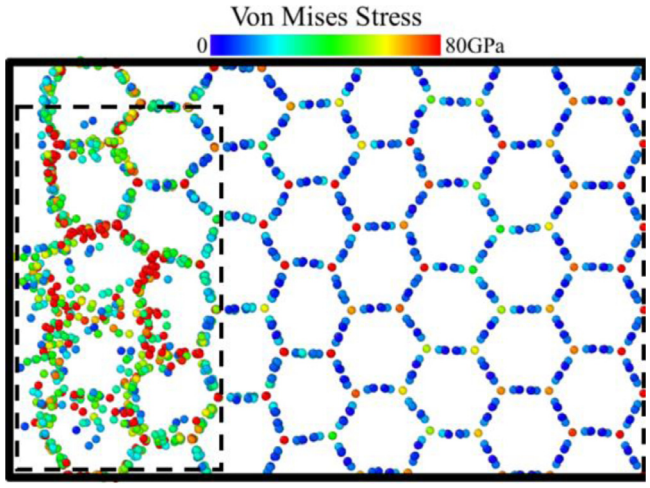

Fig. 7. Atomic structure and stress distribution of the CHC structure at 1K after the shock wave with an intensity of 0.51 eV/Å^2 (4.4km/s) propagates in the armchair direction for 1.3 ps. The local area enclosed with the dashed rectangle denotes the region where severe atomic structure distortion occurs.

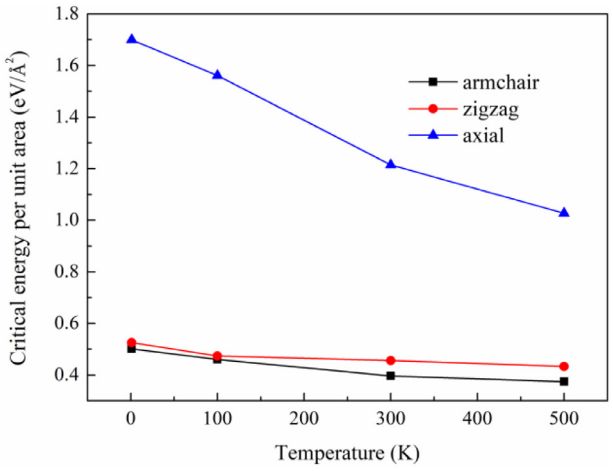

Fig. 8. Temperature dependence of the critical shock wave intensity at which structure collapse of CHC occurs.

peratures, both of which facilitate the breaking and formation of C-C bonds under the effect of the shock wave.

The critical shock wave intensity in the cell axis direction is over two times higher than those in the armchair and zigzag directions. In addition, the critical intensity in the armchair direction is lower than that in the zigzag direction, although the shock wave can propagate more easily in the armchair direction as indicated by its smaller power exponent parameter b (Fig. 3). The previous MD simulation [13] shows that the mechanical strength of CHC in different directions also follows the order of cell axis>zigzag>armchair. Hence, it can be inferred that the critical shock wave intensity is positively related to the mechanical strength of CHC.

The high critical shock wave intensity in the cell axis direction is beneficial for achieving a high EAC and limiting the penetration of the shock wave into the CHC structure to a small depth when the structure is used to shield shock waves with intensities higher than the critical value. However, when shock waves with intensities lower than the critical value are required to be shielded by the CHC structure, local structure collapse is not induced in it and the shock wave retains a high energy level as it propagates and can penetrate the CHC structure with a large depth. In this circumstance, a low wave propagation speed and a high attenuation rate are more desirable for shock wave shielding. Hence, it is advantageous to align the armchair and zigzag directions of the CHC structures with the propagation direction of the shock wave when it possesses a relatively low intensity.

It is worth noting that in the simulation model, only the atoms in the ultra-left zigzag (or armchair) line are selected to activate the shock wave in the armchair (or zigzag) direction. To investigate the effect of the size of the shock wave activation region on the shock wave attenuation in CHC, two additional simulation models are constructed in which the hexagonal rings on the ultra-left are selected as the shock wave activation region for both the shock waves propagate in the armchair and the zigzag direction (see Supplementary Fig. S6). When a larger activation region is selected, the critical shock wave intensity increases (Supplementary Fig. S7). This is because for a given intensity of the shock wave, its energy retained in the activation region after its propagation is shared by more atoms when the size of the activation region increases. The compressive deformation near the activation region reduces and the atomic stress also decreases, as shown in Supplementary Fig. S8. Consequently, the damage caused by the shock wave is mitigated when the shock wave activation region is larger. Considering the fact that the activation region selected in the present simulation is the smallest, the critical shock wave intensity shown in Fig. 8 can be considered as the lowest bound of the critical shock wave intensity of the CHC structure.

4. Conclusions

MD simulation is conducted to investigate the propagation and attenuation of shock waves in CHC. When the shock wave intensity is low, the dynamic response of the CHC structure to the shock wave is elastic and highly anisotropic. The propagation speed of shock waves in the cell axis direction of CHC is much higher than that in its armchair or zigzag direction. Under the effect of the shock wave, the atoms are first activated to displace to new positions and then vibrate there. Such vibration leads to significant interruptions of the directional propagation of the shock wave and impedes its energy transmission. In addition, the displacement and vibration amplitude are the largest when the shock wave propagates in the zigzag direction, whereas they are the smallest when the shock wave propagates in the cell axis direction, indicating that shock wave propagation in the zigzag direction is most impeded.

The characterization of the residual energy $E(x)$ of the shock wave shows that it decays with the propagation distance x in an exponential manner which can be fitted to the functional form of $E(x)=a\exp(-bx)$. The power exponent parameter b is the largest for the zigzag direction, which further proves the most rapid decay of the shock wave energy in this direction. At elevated temperatures, the residual energy decay is accelerated due to the enhanced random thermal vibration of the atoms. When cell vacancies are present in the CHC structure, its impedance to the shock wave propagation is enhanced, which is attributed to the severe deformation of the vacancies in the form of shrinkage and expansion caused by the shock wave.

The critical shock wave intensity that leads to the failure initiation of CHC is also investigated. The result indicates that the CHC structure can sustain the highest shock wave intensity in the cell axis direction, which is two times higher than those in the zigzag and the armchair directions. Considering the higher impedance of the shock wave propagation in the armchair and zigzag directions, it is beneficial to align these two directions with the propagation direction of the shock wave when its intensity is low such that its propagation in the CHC structure is slowed down. When the intensity of the shock wave is high, it is profitable to arrange the cell axis direction to the shock wave direction to fully take advantage of the high EAC of the CHC structure to prevent the penetration of the shock wave into the CHC structure.

The previous research works on the impact-resistance of advanced nanoporous structures mainly focus on their EAC, and their dynamic responses under shock loadings have seldom been reported. The results obtained in this work not only provide a deep understanding of the shock wave propagation and attenuation in CHC but are also helpful for the studies of the dynamic response of other similar impact-resistant nanoporous materials under impact loadings.

Declaration of Competing Interest

The authors declare that they have no known competing financial interests or personal relationships that could have appeared to influence the work reported in this paper.

Acknowledgments

The authors would like to acknowledge the financial support from the National Natural Science Foundation of China (No.11802087) and the high-performance computing resource from the National Supercomputing Center in Changsha.

Supplementary materials

Supplementary material associated with this article can be found, in the online version, at doi:10.1016/j.cartre.2022.100186.

References

[1] A.G. Olabi, E. Morris, M.S.J. Hashmi, Metallic tube type energy absorbers: a synopsis, Thin Walled Struct. 45 (7-8) (2007) 706–726.
[2] P.Z. Qiao, M.J. Yang, F. Bobaru, Impact mechanics and high-energy absorbing materials: review, J. Aerosp. Eng. 21 (4) (2008) 235–248.
[3] F. Xu, X. Zhang, H. Zhang, A review on functionally graded structures and materials for energy absorption, Eng. Struct. 171 (2018) 309–325.
[4] S.H. Chen, et al., Achieving high energy absorption capacity in cellular bulk metallic glasses, Sci. Rep. 5 (2015).
[5] M. Garcia-Avila, M. Portanova, A. Rabiei, Ballistic performance of composite metal foams, Compos. Struct. 125 (2015) 202–211.
[6] L.J. Gibson, M.F. Ashby, Cellular Solids: Structure and Properties, 2nd Eidtion, Cambridge University Press, 1997.
[7] L.J. Yi, et al., Giant energy absorption capacity of graphene-based carbon honeycombs, Carbon 118 (2017) 348–357.
[8] B. Sarac, J. Schroers, From brittle to ductile: Density optimization for Zr-BMG cellular structures, Scr. Mater. 68 (12) (2013) 921–924.
[9] B. Sarac, et al., Honeycomb structures of bulk metallic glasses, Adv. Funct. Mater. 22 (15) (2012) 3161–3169.
[10] N.V. Krainyukova, E.N. Zubarev, Carbon honeycomb high capacity storage for gaseous and liquid species, Phys. Rev. Lett. 116 (5) (2016) 055501.
[11] H.R. Karfunkel, T. Dressler, New hypothetical carbon allotropes of remarkable stability estimated by MNDO solid-state SCF computations, J. Am. Chem. Soc. 114 (7) (1992) 2285–2288.
[12] Z.Q. Pang, et al., Bottom-up design of three-dimensional carbon-honeycomb with superb specific strength and high thermal conductivity, Nano Lett. 17 (1) (2017) 179–185.
[13] Q. Qin, et al., Anisotropic and temperature dependent mechanical properties of carbon honeycomb, Nanotechnology 30 (32) (2019).
[14] X.K. Chen, et al., Anisotropic thermal conductivity in carbon honeycomb, J. Phys.: Condens. Matter 30 (15) (2018).
[15] Z. Zhang, et al., Nanomechanics of carbon honeycomb cellular structures, Carbon 113 (2017) 26–32.
[16] X.K. Gu, et al., On the influence of junction structures on the mechanical and thermal properties of carbon honeycombs, Carbon 119 (2017) 278–286.

[17] S.W. Wang, et al., Semimetallic carbon honeycombs: new three-dimensional graphene allotropes with Dirac cones, Nanoscale 10 (6) (2018) 2748–2754.
[18] J.P. Hu, et al., Three-dimensional honeycomb carbon: Junction line distortion and novel emergent fermions, Carbon 141 (2019) 417–426.
[19] J. Zhang, C.Y. Wang, Buckling of Carbon Honeycombs: A New Mechanism for Molecular Mass Transportation, J. Phys. Chem. C 121 (14) (2017) 8196–8203.
[20] N.V. Krainyukova, Capturing gases in carbon honeycomb, J. Low Temp. Phys. 187 (1-2) (2017) 90–104.
[21] Y. Gao, et al., Electron and phonon properties and gas storage in carbon honeycombs, Nanoscale 8 (26) (2016) 12863–12868.
[22] J.P. Hu, X.H. Zhang, Theoretical prediction of honeycomb carbon as Li-ion batteries anode material, Eur. Phys. J. B 91 (5) (2018).
[23] W.Y. Zhou, et al., A 3D porous honeycomb carbon as Na-ion battery anode material with high capacity, excellent rate performance, and robust stability, Carbon 168 (2020) 163–168.
[24] S. Plimpton, Fast Parallel Algorithms For Short-Range Molecular Dynamics, Sandia National Labs., Albuquerque, NMUnited States, 1993.
[25] A. Stukowski, Visualization and analysis of atomistic simulation data with OVITO–the Open Visualization Tool, Modell. Simul. Mater. Sci. Eng. 18 (1) (2010).
[26] D.W. Brenner, et al., A second-generation reactive empirical bond order (REBO) potential energy expression for hydrocarbons, J. Phys. Condens. Matter 14 (4) (2002) 783.
[27] G.J. Martyna, M.L. Klein, M. Tuckerman, Nosé–Hoover chains: The canonical ensemble via continuous dynamics, J. Chem. Phys. 97 (4) (1992) 2635–2643.
[28] S. Nosé, A unified formulation of the constant temperature molecular dynamics methods, J. Chem. Phys. 81 (1) (1984) 511–519.
[29] B. Li, et al., Atomistic simulations of vibration and damping in three-dimensional graphene honeycomb nanomechanical resonators, Superlattices Microstruct. 139 (2020).
[30] Y. Du, et al., Effects of cell defects on the mechanical and thermal properties of carbon honeycombs, Comput. Mater. Sci. 187 (2021).